American Mineralogist, Volume 97, pages 1219–1225, 2012

Panguite, $(Ti^{4+},Sc,Al,Mg,Zr,Ca)_{1.8}O_3$, a new ultra-refractory titania mineral from the Allende meteorite: Synchrotron micro-diffraction and EBSD

Chi Ma,[1,*] Oliver Tschauner,[1,2] John R. Beckett,[1] George R. Rossman,[1] and Wenjun Liu[3]

[1]Division of Geological and Planetary Sciences, California Institute of Technology, Pasadena, California 91125, U.S.A.
[2]High Pressure Science and Engineering Center and Department of Geoscience, University of Nevada, Las Vegas, Nevada 89154, U.S.A.
[3]Advanced Photon Source, Argonne National Laboratory, Argonne, Illinois 60439, U.S.A.

Abstract

Panguite (IMA 2010-057), $(Ti^{4+},Sc,Al,Mg,Zr,Ca)_{1.8}O_3$, is a new titania, occurring as fine-grained crystals with Ti-rich davisite in an ultra-refractory inclusion within an amoeboid olivine inclusion from the Allende CV3 carbonaceous chondrite. The phase was characterized by SEM, EBSD, synchrotron micro-diffraction, micro-Raman spectroscopy, and EPMA. The mean chemical composition of the type panguite is (wt%) TiO_2 47.97, ZrO_2 14.61, Sc_2O_3 10.67, Al_2O_3 7.58, MgO 5.54, Y_2O_3 5.38, CaO 3.34, SiO_2 1.89, FeO 1.81, V_2O_3 0.95, Cr_2O_3 0.54, HfO_2 0.28, sum 100.56 with a corresponding empirical formula calculated on the basis of 3 O atoms of $[(Ti_{0.79}Zr_{0.16}Si_{0.04})^{4+}_{\Sigma 0.99}(Sc_{0.20}Al_{0.20}Y_{0.06}V_{0.02}Cr_{0.01})^{3+}_{\Sigma 0.49}(Mg_{0.18}Ca_{0.08}Fe_{0.03})^{2+}_{\Sigma 0.29}]_{\Sigma 1.77}O_3$. Synchrotron micro-Laue diffraction (i.e., an energy scan by a high-flux X-ray monochromatic beam and white beam diffraction) on one type domain at sub-micrometer resolution revealed that panguite is an orthorhombic mineral in space group *Pbca*. The structure is a subgroup of the *Ia*3 bixbyite-type. The cell parameters are $a = 9.781(1)$, $b = 9.778(2)$, and $c = 9.815(1)$ Å, yielding $V = 938.7(1)$ Å^3, $Z = 16$, and a calculated density of 3.746 g/cm^3. Panguite is not only a new mineral, but also a new titania material, likely formed by condensation. It is one of the oldest minerals in the solar system.

Keywords: Panguite, $(Ti^{4+},Sc,Al,Mg,Zr,Ca)_{1.8}O_3$, new ultra-refractory mineral, new titania, Allende meteorite, CV3 carbonaceous chondrite, synchrotron micro-diffraction, EBSD

Introduction

During a nano-mineralogy investigation of the Allende meteorite at Caltech, a new titania mineral $(Ti^{4+},Sc,Al,Mg,Zr,Ca)_{1.8}O_3$, named "panguite," was identified in an ultra-refractory inclusion within an amoeboid olivine inclusion (AOI). Electron probe microanalysis (EPMA), high-resolution scanning electron microscope (SEM), electron backscatter diffraction (EBSD), synchrotron micro-Laue diffraction with subsequent energy scans, and micro-Raman spectroscopic analyses were used to determine its composition, physical properties, and structure and to characterize associated phases. Synthetic $(Ti^{4+},Sc,Al,Mg,Zr,Ca)_{1.8}O_3$ is not known. Thus, panguite is not only a new mineral and a new phase to meteoritics, but it is also a new material. In this work, we describe the first occurrence of panguite in nature, as a new ultra-refractory oxide among the oldest solid materials in the solar system. Preliminary results are given in Ma et al. (2011a).

Mineral name and type material

The mineral and the mineral name (panguite) have been approved by the Commission on New Minerals, Nomenclature and Classification (CNMNC) of the International Mineralogical Association (IMA 2010-057). The name panguite is for Pan Gu, the giant in ancient Chinese mythology, who created the world by separating the heaven and earth from chaos in the beginning, in allusion to the mineral with an ultra-refractory origin being among the first solid materials in the solar system. Holotype material (Section MC2Q of Caltech specimen Allende12A) is deposited under catalog USNM 7602 in the Smithsonian Institution's National Museum of Natural History, Washington, D.C., U.S.A.

Occurrence

The Allende meteorite fell in and near Pueblito de Allende, Chihuahua, Mexico, on February 8, 1969 (Clarke et al. 1971). It is a CV3 carbonaceous chondrite and the study of objects in this meteorite has had a tremendous influence on current thinking about processes, timing, and chemistry in the primitive solar nebula and small planetary bodies. The mineral panguite was found within one irregular ultra-refractory inclusion in one polished section (USNM 7602), prepared from a ~1 cm diameter Allende fragment (Caltech Meteorite Collection No. Allende12A). The host refractory inclusion is about 30 × 20 μm in size in the section plane and resides within an AOI, surrounded by a matrix of mostly fine-grained olivine and troilite. Panguite occurs with Ti-rich davisite and minor Sc-Ti-bearing diopside in the refractory inclusion (Figs. 1–2). Davisite appears to be the common thread for panguite. We have observed this phase in two additional inclusions, one from Allende and the other from the CM chondrite Murchison (Ma et al. 2011b). In both cases, panguite is invariably in contact with davisite. Moreover, Zhang and Hsu (2009) described a phase from the CH chondrite SaU 290, which we have confirmed by EBSD and EPMA at Caltech to be another example of panguite (see their Fig. 6c) and their grains are also in contact with davisite. Given

* E-mail: chi@gps.caltech.edu

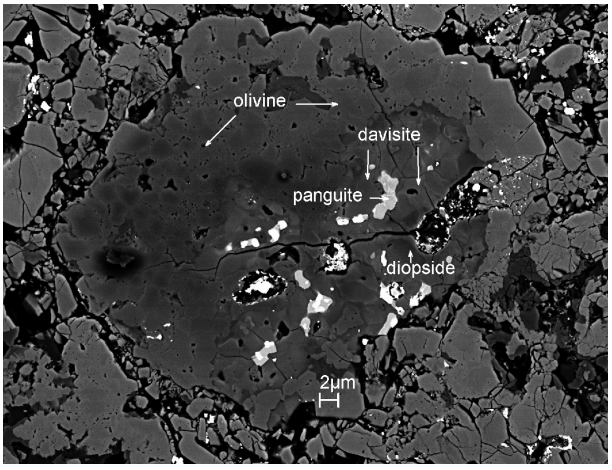

FIGURE 1. Backscatter electron image of the ultra-refractory inclusion within an Allende AOI in section USNM 7602.

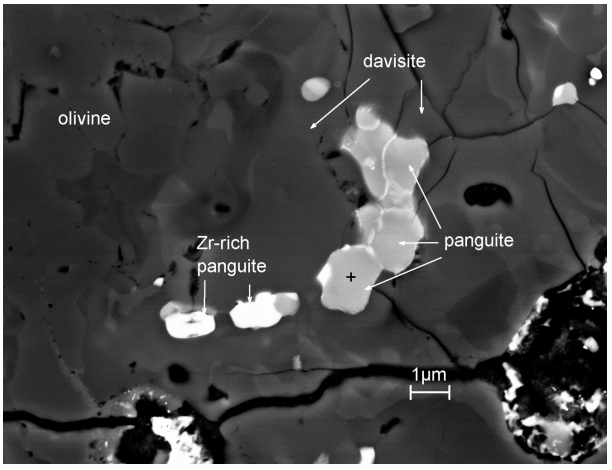

FIGURE 2. Enlarged backscatter image showing the area where panguite crystals (type material) occur with smaller Zr-rich panguite in davisite (Fig. 1). The cross marks where the EBSD pattern (shown in Fig. 3) and the synchrotron micro-diffraction data were collected. The mottled appearance of the davisite mostly reflects differences in Sc concentrations.

the occurrence in multiple meteorites of variable type (CH, CM, CV), we conclude that panguite is a rare but widespread constituent of carbonaceous chondrites and, given the consistent association with davisite, we conclude that the origin of panguite is intimately connected to the origin and evolution of davisite.

APPEARANCE, PHYSICAL AND OPTICAL PROPERTIES

Panguite occurs as irregular to subhedral grains, 500 nm to 1.8 μm in size. In section, panguite is opaque. Color, streak, luster, hardness, tenacity, cleavage, fracture, density, and refractive index were not determined because of the small grain size. The density, calculated from the empirical formula, is 3.746 g/cm^3. It is non-fluorescent under the electron beam of a scanning electron microscope, and we observed no crystal forms or twinning. Two distinct chemistries are observed for panguite, and this is readily appreciated through atomic number (*Z*) contrast in BSE images. The larger panguite grains shown in Figure 2 (lighter gray), which constitute the type material, are much lower in the high-*Z* elements Zr and Y than are some of the smaller grains (white in Fig. 2).

CHEMICAL COMPOSITION

Chemical analyses of panguite (on the larger grains in Fig. 2) and associated minerals were carried out using a JEOL 8200 electron microprobe (WDS mode, 10 kV, 5 nA beam in focused mode). Standards for the analysis were TiO_2 (Ti*K*α, O*K*α), zircon (Zr*L*α), $ScPO_4$ (Sc*K*α), synthetic anorthite (Ca*K*α, Al*K*α, Si*K*α), forsterite (Mg*K*α), YPO_4 (Y*L*α), fayalite (Fe*K*α), V_2O_3 (V*K*α), Cr_2O_3 (Cr*K*α), and Hf metal (Hf*L*α). Quantitative elemental microanalyses were processed with the CITZAF correction procedure (Armstrong 1995) and analytical results are given in Table 1. Repeated electron probe analysis of panguite with and without O being explicitly measured gave similar results, implying that Ti in the structure is mostly 4+. Moreover, the sum of quadrivalent cations per formula unit in panguite is invariably 1.0 if the Ti is assumed to be only 4+. The oxidation state of Fe is unknown because the concentrations are so much lower than for Ti and we arbitrarily assume that it is divalent. The empirical formula of type panguite (based on O = 3) is: $[(Ti_{0.79}Zr_{0.16}Si_{0.04})^{4+}_{\Sigma 0.99}(Sc_{0.20}Al_{0.20}Y_{0.06}V_{0.02}Cr_{0.01})^{3+}_{\Sigma 0.49}(Mg_{0.18}Ca_{0.08}Fe_{0.03})^{2+}_{\Sigma 0.29}]_{\Sigma 1.77}O_3$, where the oxidation states of Ti and Fe are assumed to be 4+ and 2+, respectively. The general formula is $(Ti^{4+},Sc,Al,Mg,Zr,Ca)_{1.8}O_3$, expressed as $(Ti^{4+},Sc,Al,Mg,Zr,Ca,\square)_2O_3$ or $(Ti^{4+},Sc,Al,Mg,Zr,Ca)_3O_5$.

Associated Zr-rich panguite has an empirical formula $[(Ti_{0.56}Zr_{0.31}Si_{0.12})^{4+}_{\Sigma 0.99}(Al_{0.17}Sc_{0.13}Y_{0.13}V_{0.01})^{3+}_{\Sigma 0.44}(Ca_{0.23}Mg_{0.07}Fe_{0.05})^{2+}_{\Sigma 0.35}]_{\Sigma 1.78}O_3$ and coexisting davisite has a mean composition of $(Ca_{0.99}Mg_{0.01})_{\Sigma 1.00}[(Sc_{0.35}Ti_{0.25}V_{0.01}Y_{0.01}Al_{0.01})^{3+}_{\Sigma 0.63}(Mg_{0.19}Fe_{0.04})^{2+}_{\Sigma 0.23}(Ti_{0.12}Zr_{0.03})^{4+}_{\Sigma 0.15}]_{\Sigma 1.01}(Si_{1.07}Al_{0.93})_{\Sigma 2.00}O_6$, with partitioning of Ti^{3+} and Ti^{4+} based on a stoichiometric formula unit containing 4.00 cations and 6 O atoms. Note that about two thirds of the Ti is inferred to be trivalent in davisite that coexists with panguite containing little if any Ti^{3+}. Minor isolated Sc-Ti-rich diopside (Table 1) occurs in the inclusion. Fine-grained (~250

TABLE 1. The mean electron microprobe analytical result for type panguite, Zr-rich panguite, davisite, diopside, and surrounding olivine

Constituent	Type panguite	Zr-rich panguite	Davisite	Diopside	Olivine
wt%	n = 5*	n = 4	n = 4	n = 3	n = 4
TiO_2	47.97(1.09)†	30.68(31)	12.74(39)	7.04(95)	0.12(5)
ZrO_2	14.61(86)	25.92(22)	1.53(27)	0.79(45)	b.d.
Sc_2O_3	10.67(25)	5.97(20)	10.16(97)	3.90(1.37)	b.d.
Al_2O_3	7.58(22)	5.94(38)	20.29(1.56)	11.53(1.74)	0.12(7)
MgO	5.54(55)	1.98(7)	3.43(84)	11.15(1.74)	35.47(1.71)
Y_2O_3	5.38(37)	10.16(28)	0.41(10)	0.50(23)	b.d.
CaO	3.34(40)	8.73(47)	23.54(8)	24.72(49)	0.17(3)
SiO_2	1.89(18)	5.04(31)	27.34(1.49)	40.75(2.94)	37.99(21)
FeO	1.81(25)	2.21(29)	1.07(15)	1.25(4)	26.84(1.35)
V_2O_3	0.95(14)	0.27(6)	0.47(2)	0.18(8)	b.d.
Cr_2O_3	0.54(13)	b.d.‡	b.d.	b.d.	b.d.
HfO_2	0.28(7)	0.34(12)	b.d.	b.d.	b.d.
Total	100.56	97.24	100.98	101.81	100.71

* Number of analyses.
† Numbers in parentheses represent one standard deviation of the mean for the n analyses conducted on the phase.
‡ Below detection. Detection limits at 99% confidence are Cr 0.15 wt%, Hf 0.18%, Zr 0.15%, Sc 0.07%, and Y 0.28%.

nm) Ru-Ir-Mo-Fe-Os alloys are scattered throughout the refractory portion of the inclusion; most appear to be included in davisite but some may be located along grain boundaries and a few are in contact with panguite. The compositions of two grains by SEM-EDS are $Ru_{0.30}Ir_{0.29}Mo_{0.17}Fe_{0.13}Os_{0.11}$ and $Ru_{0.32}Ir_{0.15}Os_{0.14}Fe_{0.14}Mo_{0.14}Ni_{0.07}W_{0.03}$. The surrounding olivine is $Fa_{30}Fo_{70}$ (Table 1) with scattered Fe-Ni alloy. If panguite and davisite equilibrated with each other, the compositions imply that Ti^{4+}, Zr, V, and Y are strongly partitioned into panguite relative to davisite and Ca and, to a lesser extent, Al in davisite relative to panguite. Zr-rich panguite has lower Sc (2x) than panguite but higher Y (by 2x) implying a significantly higher mean radius for the trivalent cations (0.78 vs. 0.68 Å), suggesting that Zr-rich panguite may be able to accommodate higher concentrations of the REE.

CRYSTALLOGRAPHY

EBSD and synchrotron micro-Laue diffraction

EBSD analyses at a submicrometer scale were performed on the vibro-polished section using methods described in Ma and Rossman (2008a, 2009a). An HKL EBSD system on a ZEISS 1550VP scanning electron microscope was used for these measurements and operated at 20 kV and 6 nA in a focused beam configuration with a 70° tilted stage and variable pressure (20 Pa) mode, which allows the study of uncoated specimens. The structure was constrained by comparing the observed EBSD pattern with those of perovskite [$CaTiO_3$] (Liu and Liebermann 1993), armalcolite [$(Mg,Fe)Ti_2O_5$] (Wechsler 1977), pseudobrookite [Fe_2TiO_5] (Yang and Hazen 1999), tistarite [Ti_2O_3] (Vincent et al. 1980), Ti_3O_5 (Onoda 1998), Sc_2TiO_5 (Kolitsch and Tillmanns 2003), TiO_2 structures (Ballirano and Caminiti 2001; Howard et al. 1991; Meagher and Lager 1979), Sc_2O_3 (Schleid and Meyer 1989), and tazheranite [$(Zr,Ti,Ca)O_{1.75}$] (cubic zirconia; Rastsvetaeva et al. 1998). Of these, EBSD patterns of the new phase can be matched using the $Ia\bar{3}$ structure of Sc_2O_3 or the *Fm*3*m* structure of tazheranite, suggesting a cubic structure, which assisted us in characterizing its bixbyite-related structure by synchrotron analysis.

Synchrotron micro-Laue diffraction on one titania grain was carried out at the 34ID-E undulator beamline of the Advanced Photon Source in the Argonne National Laboratory using a 250 × 400 nm^2 polychromatic X-ray beam and an array of Perkin-Elmer amorphous Si area detectors. Micro-Laue diffraction is an important tool in examining orientation and strain in polycrystalline samples down to micrometer-scale grain sizes (Liu et al. 2011, 2004; Tamura et al. 2005). Moreover, it has been successfully used for identification of crystalline phases (Tamura et al. 2002). In principle, the combination of white beam Laue diffraction with subsequent diffraction by a monochromatic beam tuned over an extended range of energy can yield an excellent tool in analyzing structures of phases occurring only in micrometer-scale grains (such as the present new mineral). First, the Laue pattern is indexed. Subsequent scans of energy are established by tuning a monochromator and simultaneously the gap of an undulator, which allows for identification of the Q-vectors for each of the indexed reflections. For micrometer-scale specimens, this technique has decisive advantages over monochromatic single-crystal diffraction techniques. The specimen does not need to be rotated and, consequently, the circle of confusion of the goniometer does not affect the intensities of measured reflections and reflection coordinates. Hence, the combination of Laue diffraction with energy-scans permits, in principle, structure analysis from individual crystallites on a micrometer to submicrometer scale. However, this technique is still in an early developmental stage, and we encountered several technical problems during data evaluation. For the present set of data, the correlation of crystal orientation derived from the Laue pattern indexing and Q-values of reflections from the energy-scans is not conserved and the latter had to be re-indexed based on their *d*-spacings (see below). Moreover, the change of the diffraction volume with changing energy could not be corrected and we were consequently constrained to sampling only a limited energy range. Corrections for polarization and absorption were applied and the background was fitted and subtracted for each reflection observed in the energy-scans. Here, we describe our procedures for data collection and evaluation. The sample location was identified by microbeam X-ray fluorescence mapping of Ti, Zr, Fe, and by subsequent Laue diffraction. Laue diffraction was also used to identify individual titania crystallites. A monochromatic beam energy scan between 16.5 and 24 keV with increments of 3 eV was conducted on one panguite single-crystal domain with a primary beam focused to 250 × 400 nm^2. The set of Q-values indicate a weak orthorhombic distortion of the cubic cell suggested by the EBSD patterns and a unit cell larger than that expected of a fluorite structure. Anion deficient AB_2 compounds with ratio of ionic radii compatible with the fluorite structure often assume structures closely related to fluorite but of larger unit cells such as the bixbyite- and the pyrochlor-structures. We modeled orthorhombic distorted fluorite-, pyrochlore-, and bixbyite cells of $Ti_{1.8}O_3$ using subgroups of the cubic aristotype cells and found a good agreement between the observed reflections and an orthorhombic distortion of the bixbyite type model. The set of observed reflections does not indicate a non-primitive Bravais lattice. Trial indexing with Jade 6.5 also indicated cell shapes compatible with a primitive orthorhombic distorted cell of dimensions compatible with a bixbyite-type structure. Based on the indices from trial indexing and subsequent cell refinement with UnitCell (Holland and Redfern 1997), we established a set of 17 unique reflections (Deposit Table 1[1]), which we used for a "local optimization" of the structure model based on the reversed Monte Carlo algorithm of Endeavor (Putz et al. 1999). Fractional coordinates of atoms in the initial structure model were taken from the structure of Sc_2O_3 (Bartos et al. 1993) transformed to the *Pbca* subgroup (see below). The optimization converged to an R_{Bragg}-factor of 0.06. Subsequently, fractional coordinates, cation occupancies, and isotropic thermal displacement factors were refined to an R_1 of 0.07 using SHELXL (Sheldrick 2008) (Table 2, Deposit CIF file[1]). Hereby, we refined cation occupancies, U_{iso} of cations, U_{iso} of anions, then the cation and anion fraction coordinates in groups T1 + Ti2, Ti3 + Ti4, then the first

[1] Deposit item AM-12-043, Deposit Tables and CIF. Deposit items are available two ways: For a paper copy contact the Business Office of the Mineralogical Society of America (see inside front cover of recent issue) for price information. For an electronic copy visit the MSA web site at http://www.minsocam.org, go to the *American Mineralogist* Contents, find the table of contents for the specific volume/issue wanted, and then click on the deposit link there.

three and the second three sets of O fractional coordinates. We did not refine all fractional coordinates simultaneously. All but the *y*- and *z*-coordinates of O6 refined without large shifts. We note that O6 and, to a lesser extent, O1 have an unusually large thermal displacement factor, whereas the factors of all other ions are in a range expected for a vacancy-stabilized structure.

In bixbyite, the cations assume two Wyckoff sites, 8*a* and 24*d*, and the anion resides on the general position 48*c*. The cubic bixbyite structure is related to the present primitive orthorhombic cell by a group-subgroup chain $Ia\bar{3} \rightarrow Ibca \rightarrow Pbca$ and the sites are mapped as follows: $8a \rightarrow 8a \rightarrow 8c$, which is the general position in *Pbca*, $24d \rightarrow 8c + 8c + 8d \rightarrow 8c + 8c + 8c$, $48e \rightarrow 16f + 16f + 16f \rightarrow 8c$ (six times) (Aroyo et al. 2006). Hence in panguite, all atoms reside on general positions. Vacancy-distribution varies little among the four cation sites (Table 2). Partial or full ordering of the cations among the four available sites is not supported by the data. In all possible cases of such ordering, the R_{Bragg} and R_1 increase to between 0.084 and 0.19 and 0.11 to 0.12, respectively. However, a combined correlation in occupancies of Zr plus Y and Al plus Mg or Si or vacancies on the same site cannot be excluded because the contributions to the combined form factors cancel each other on a level comparable to the uncertainties of the structure model. On the other hand, correlation between ions of small and large radii or divalent and tetravalent ions can be expected but does not seem to occur in panguite on a length scale sampled by X-ray diffraction. The orthorhombic distorted bixbyite cell of $Ti_{1.8}O_3$ was used to calculate an EBSD pattern and compared to the observed patterns. The EBSD patterns of type panguite and Zr-rich panguite can be indexed best by the *Pbca* structure (Fig. 3), with mean angular deviations as low as 0.3. EBSD patterns of panguite consist of Kichuchi bands without fine details, consistent with a random distribution of cations on the four different cation sites.

In sum, panguite assumes a cation-deficient bixbyite-type structure with an orthorhombic distortion to space group *Pbca* with unit-cell dimensions: $a = 9.781(1)$, $b = 9.778(2)$, $c = 9.815(1)$ Å, $V = 938.7$ (1) Å^3, and Z = 16. X-ray powder-diffraction data (Deposit Table 2[1], in angstrom for Cu$K\alpha_1$, in Bragg-Brentano geometry) were calculated from the cell parameters with the empirical formula from this study using PowderCell version 2.4 (Kraus and Nolze 1996).

Panguite establishes an interesting case of symmetry-reduction as consequence of lattice relaxation due to a large density of vacancies. It is interesting to compare panguite to orthorhombic α-Mn_2O_3 that, in terms of symmetries, deviates from panguite only by having two cations residing on sites 4*a* and 4*b* rather than joining a general site (Table 2) (Geller 1971). Deviations of the panguite- and the α-Mn_2O_3-structure from the cubic aristotype (in both cases the bixbyite-type structure) can be quantified in terms of the amplitudes of condensing modes, which generate the observed static distortion. The character and number of these modes can be derived by the group-subgroup relation between the cubic and the orthorhombic phase and by the consequent splitting of occupied Wyckoff sites (see above). We derived a cubic aristotype structure by mapping the panguite cell onto $Ia\bar{3}$. Amplitudes, character, and number of condensing modes were derived using Amplimodes (Orobengoa et al. 2009; Perez-Mato et al. 2010).

TABLE 2. Atomic coordinates of panguite structure

	x/a	*y/b*	*z/c*	SOF	U_{iso}
Ti1	0.4791(3)	0.0353(1)	0.333(2)	0.86(1)	0.0602(2)
Ti2	0.0080(3)	0.2474(8)	0.462(1)	0.81(1)	0.0687(1)
Ti3	0.24626(6)	0.47104(5)	0.000023(2)	0.87(1)	0.0669(4)
Ti4	0.246(1)	0.2533(7)	0.2477(6)	0.80(3)	0.0568(5)
O1	0.393(15)	0.15(12)	0.38(6)	1	0.2(1)
O2	0.4249(4)	0.433(2)	0.198(2)	1	0.071(1)
O3	0.1400(1)	0.3764(1)	0.3940(2)	1	0.0346(4)
O4	0.0997(4)	0.35109(1)	0.1087(9)	1	0.042(2)
O5	0.108(2)	0.1106(5)	0.353(3)	1	0.059(1)
O6	0.351(9)	0.11(2)	0.1(1)	1	0.2(1)

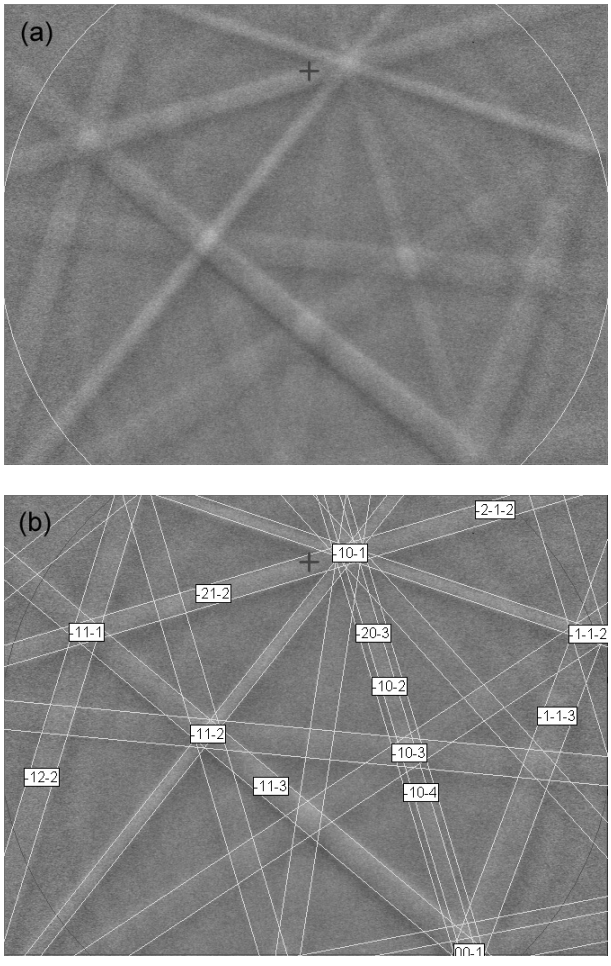

FIGURE 3. (**a**) EBSD pattern of the labeled panguite crystal (marked with a cross) in Figure 2. (**b**) The pattern indexed with the *Pbca* structure using the cell from synchrotron micro-diffraction.

There are two sets of condensing zone center modes in direction **a** (Γ_1^+) and **a**+**b** ($\Gamma_2^+ + \Gamma_3^+$), respectively. They correspond to an isostructural mechanism and to a reduction of symmetry to subgroup *Ibca*, respectively. Furthermore, there are two sets of condensing modes at the H-point of the Brillouin-zone, which also point along **a** (H_1^+) and **a**+**b** ($H_2^+ + H_3^+$) and correspond to a reduction in symmetry to subgroups $Pa\bar{3}$ and *Pbca*, respectively. The latter mechanism is driving the transition to the observed space group. For panguite we find a total distortion amplitude (the amplitude of the sum of all condensing mode vectors) of

3.68 Å with atomic displacements ranging from 0.05 to 0.89 Å. In panguite and α-Mn_2O_3, the total distortion amplitude is 2.81 Å and atomic displacements range from 0.00 to 0.50 Å.

In α-Mn_2O_3 the Γ_1^+ and H_1^+-modes have the largest amplitudes with values of 2.21 and 1.63 Å, respectively, whereas the two other mechanisms have amplitudes of less than 0.5 Å. Panguite behaves almost complementary, having $H_2^+ + H_3^+$ and Γ_1^+ dominating with amplitudes of 2.51 and 1.82 Å, respectively; the two other mechanisms have amplitudes of 1.26 and 1.53 Å. When looking at the contributions of individual atom to these modes, we find that shifts of cations in panguite are generally smaller than shifts of Mn in α-Mn_2O_3. On the other hand, shifts of O-positions are greater in panguite than in α-Mn_2O_3. In sum, the following picture emerges. In panguite and α-Mn_2O_3, the same mode condensation processes are active. However, in both phases, the modes that are dominating the distortions from the cubic aristotype are different. The spin ordering in α-Mn_2O_3 seems to be consistent with cubic supercell formation by condensation of Γ_1^+ and H_1^+, whereas the orthorhombic distortion is minor and appears to be mostly the result of rearranging the O-sublattice according to the changed valence electronic states of Mn. This is at least suggestive because we see the distortive $H_2^+ + H_3^+$ mode being dominant in panguite where magnetic interactions are absent. In panguite, the structural distortion is related to the high density of vacancies and subsequent lattice-relaxation. Thus, this distortion may be labeled as a symmetry-controlled partial collapse of the O-sublattice while the cation-sublattice experiences smaller deformation. In accordance with the high density of vacancies on the cation sites and collapse of the O-sublattice (Table 2), the total amplitude of distortion in panguite is 30% larger than the magnetostrictive distortion in α-Mn_2O_3.

Raman spectroscopy

Raman spectroscopic microanalysis was carried out using a 514.5 nm laser in a Renishaw M1000 micro-Raman spectrometer system on domains of the sample in the polished section previously identified as panguite crystals through SEM imaging and EBSD analyses. Methods are described in Ma and Rossman (2008a, 2009a). Approximately 5 mW of 514.5 nm laser illumination (at the sample) focused with a 100× objective lens provided satisfactory spectra. The spot size was about 2 μm (i.e., roughly the size of the largest crystals). Peak positions were calibrated against a silicon standard. A dual-wedge polarization scrambler was used in the laser beam for all spectra to reduce the effects of polarization.

Raman microanalyses show that the spectrum of panguite has two major peaks, at 380 and 405 cm^{-1}. There are additional weak features but these may at least partially reflect the surrounding Ti-rich davisite, as shown in Figure 4. We used the orthorhombic bixbyite-like structure of $Ti_{1.8}O_3$, as described above, to calculate the Raman spectrum with the valence bond method using the Vibratz software (Dowty 1987). Force constants were estimated based on earlier comparative studies of bixbyite-type scandium- and rare-earth sesquioxides (Ubaldini and Carnasciali 2008) and subsequently refined based on the observed energies of Raman shifts in panguite (Dowty 1987). We processed the observed Raman spectrum by removing the background and subtracting the spectrum of adjacent davisite, although complete removal of Raman features of davisite may not be achieved. Figure 5 shows a comparison of the calculated and observed Raman spectrum of panguite. Observed relative intensities were matched fairly well by computing only the A_g modes in XX scattering geometry and the energy of the pronounced doublet at 380 and 405 cm^{-1} is reproduced to within 5 cm^{-1}. This doublet is the result of orthorhombic (pseudotetragonal) distortion of the cell. In cubic Sc_2O_3 and Y_2O_3, the Raman spectrum is similarly strong, dominated by a single Raman shift at 420 and 380 cm^{-1}, respectively (Ubaldini and Carnasciali 2008). A set of seven force constants for cation-oxygen stretching vibrations and two force constants for O-O repulsion was used to model the spectrum of Ti_2O_3 in the panguite-structure. All cation-anion bond force constants contribute to the normal modes, which generate the Raman shifts at 380 and 405 cm^{-1}. The force constants were optimized to values between 0.90 to 1.08 mdyn/Å with an average of 0.97 mdyn/Å, thus falling well within the range of force constants

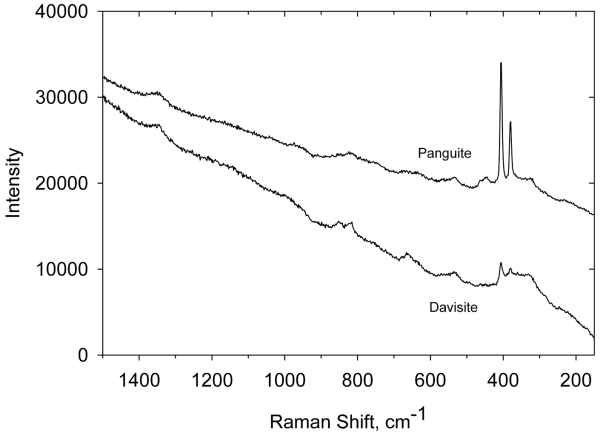

FIGURE 4. Micro-Raman spectra of panguite and associated davisite in the refractory inclusion, collected under identical conditions, showing absolute intensities. The spectra are offset vertically for clarity of display.

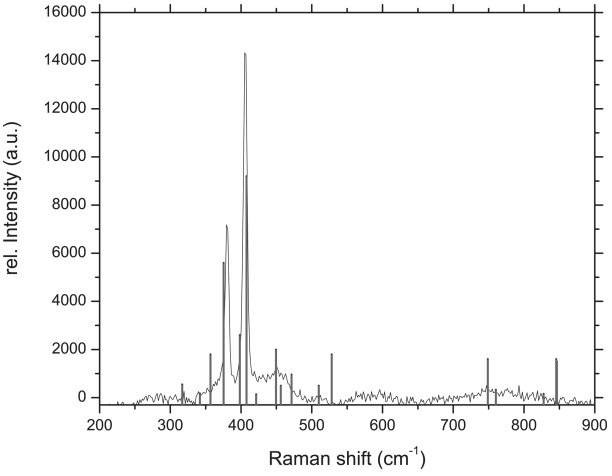

FIGURE 5. Comparison of a calculated and observed Raman spectrum of panguite. The spectrum of panguite shown in Figure 4 was processed by subtraction of background and of a spectrum of davisite. Gray bars: Calculated spectrum of panguite. Only A_g modes are shown and intensities represent an XX scattering geometry.

observed for rare-earth sesquioxides of the bixbyite type and sensibly extending the observed correlation of cation-anion bond stretching force constants and lattice parameters in bixbyite-type rare-earth and Sc_2O_3 (Ubaldini and Carnasciali 2008). To that purpose, we consider the relation connecting force constants, cation-anion distance, molar volume, and bond compressibility (Born and Huang 1954). In an ionic bond model, the inverse square of the cation-anion distance should be a linear function of the ratio of force constant and molar volume. Within the limit of this bond model, the slope of the correlation corresponds to the ration of the elastic bulk modulus and the coordination number. Figure 6 shows that the correlation between these parameters is linear for several lanthanide oxides, yttria, scandia, and panguite. The excellent correlation indicates that the bixbyite-type oxides, including panguite, have predominantly ionic bonding and the slope yields the ratio of cation coordination number and bond compressibility (Born and Huang 1954). We note that the average slope for the linear regression in Figure 6 yields an inverse bond compressibility of 202 GPa, which accords reasonably well with reported bulk moduli for of 149.5 GPa for Y_2O_3 149.5 and 188 GPa for Sc_2O_3 (Palko et al. 2001; Barzilai et al. 2011).

Discussion

Zirconium is a key element in deciphering some of the earliest and most extreme environments before and during formation of the solar system because its oxide is highly refractory in both reducing and oxidizing gases (Lodders 2003), and it holds isotopic clues to nucleosynthetic contributions to the solar system and how they were introduced (Nicolussi et al. 1997). Various Zr-, Y-, Sc-rich oxides and silicates (e.g., Allen et al. 1980; Hinton et al. 1988; El Goresy et al. 2002), including davisite [$Ca(Sc,Ti^{3+},Ti^{4+},Mg)SiAlO_6$; Ma and Rossman 2009b], allendeite ($Sc_4Zr_3O_{12}$; Ma et al. 2009), tazheranite [$(Zr,Ti,Ca,Y)O_{1.75}$; Ma and Rossman 2008b], thortveitite ($Sc_2Si_2O_7$; Ma et al. 2011b), lakargiite ($CaZrO_3$; Ma 2011), and panguite (this study), have been reported in refractory inclusions. Panguite is particularly interesting as a potential sensor of environment because it is a titanate that contains significant concentrations of Al (ionic radius in octahedral coordination of 0.535Å), Sc (0.745Å), and Y (0.90Å), so it should also be able to readily accept large concentrations of Ti^{3+} (0.67Å) and the heavy rare earths (HREE). Based on oxygen analyses and stoichiometric considerations (e.g., the fact that tetravalent cations consistently sum to 1.0 in a formula unit with 3 O atoms if all Ti is treated as tetravalent), nearly all of the Ti in type panguite is 4+. The absence of measurable Ti^{3+} in our Allende panguite, therefore, strongly suggests that these crystals equilibrated in an oxidizing environment. Yet they coexist with davisite that has Ti^{3+}/Ti^{4+}~2, strongly suggesting reducing conditions. This intimate juxtaposition of oxidized and reduced phases (Fig. 2) is thematically similar to the presence in type B inclusions of Ti^{4+}-enriched spinels hosted by Ti^{3+}-enriched clinopyroxene (Paque et al. 2010). Zr-Y-Sc enriched phases are, however, likely to provide more direct clues to the source of extravagant dichotomies in redox conditions because they contain many more independent constraints on their environment.

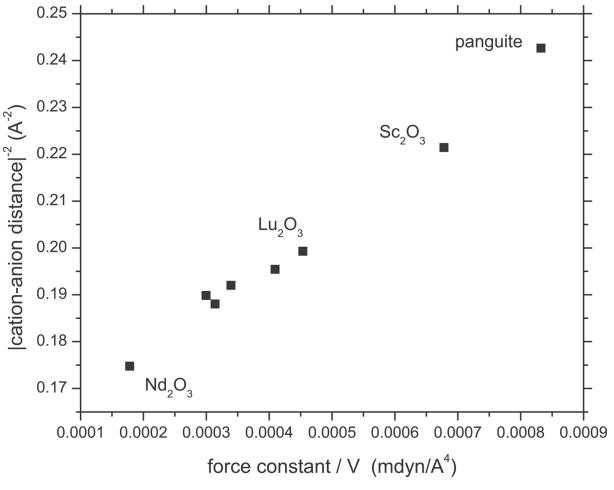

Figure 6. Plot of the inverse square of the cation-anion distance vs. the ratio of force constant and molar volume. Data for five lanthanide sesquioxides, scandia, and yttria are taken from Ubaldini and Carnasciali (2008). Variation in slope is from deviations from an ionic bond model.

Panguite has not been synthesized to our knowledge. Nor have the thermodynamic properties been characterized experimentally and it is, therefore, difficult to quantify formation conditions for this phase. Nevertheless, since the type panguite occurs with davisite in the refractory core of an amoeboid olivine inclusion, we can reasonably place some constraints on the origin of panguite through an exposition of the key genetic features of AOIs. In amoeboid olivine inclusions from meteorites that have largely escaped the preterrestrial alteration processes endemic to Allende (e.g., CR chondrites), the olivine is highly magnesian (<Fa_2) and included phases are essentially FeO-free (e.g., Krot et al. 2004). The oxygen isotopic compositions are similar to those observed in Ca-,Al-rich inclusions (CAIs, e.g., Aléon et al. 2002; Hiyagon and Hashimoto 1999). In Allende, the olivine in AOIs is variable in Fe content and the oxygen isotope compositions are also variable, with $\delta^{18}O$ of the most magnesian olivines comparable to values expected of CAIs and fayalitic olivines much more variable and generally much less enriched in ^{16}O. These features can be attributed to the incomplete but pervasive alteration of Allende. Olivine surrounding the type inclusion is relatively Fe-rich (Fa_{21}) and it is, therefore, quite likely that the small amount of Fe observed in the type panguite is secondary. The reactions involved in the substitution (e.g., exchange with Mg as in Allende spinels and olivine vs. participating in an oxidation reaction involving Ti^{3+}) are unknown but the consistent near unity number of cations of Ti + Zr per 3 O atoms and the likely ability of the phase to accommodate Ti^{3+}, if available, suggests that the Ti was predominately tetravalent prior to parent body alteration. The conditions of formation for the type panguite were oxidizing relative to the highly reducing conditions expected for a gas of solar composition or of C-rich vapors generally associated with the formation of presolar SiC and graphite. The Ti^{3+}-bearing davisite that encloses panguite also implies highly reducing conditions and it may be that davisite nucleated opportunistically on panguite that had grown previously under oxidizing conditions. If so, davisite and panguite, although strongly associated, may not be genetically related.

Panguite is not only a new titania mineral formed in the solar nebula, but also a new material, representing a case of symmetry-

reduction as consequence of lattice relaxation due to the large number of vacancies. This high defect density and the presence of Ti^{4+} and Sc^{3+} make panguite an interesting candidate for high ion conductivity at elevated temperature.

ACKNOWLEDGMENTS

SEM, EBSD, and EPMA analyses were carried out at the Caltech GPS Division Analytical Facility, which is supported, in part, by NSF Grants EAR-0318518 and DMR-0080065. Synchrotron micro-diffraction was carried out at the 34ID-E beamline of the Advanced Photon Source. Use of the Advanced Photon Source, an Office of Science User Facility operated for the U.S. Department of Energy (DOE) Office of Science by Argonne National Laboratory, was supported by the U.S. DOE under Contract no. DE-AC02-06CH11357. This research was also supported by NNSA Cooperative Agreement DE-FC88-01NV14049, NASA OSS Grant NNX-09AG40G, and NSF Grant EAR-0947956. We thank Aicheng Zhang for bringing the CH chondrite SaU 290 to Caltech for EBSD and EPMA study. We thank Irina Galuskina, Vladimir Bermanec, and Fernando Colombo for their helpful reviews.

REFERENCES CITED

Aléon, J., Krot, A.N., and McKeegan, K.D. (2002) Calcium-aluminum-rich inclusions and amoeboid olivine aggregates from the CR carbonaceous chondrites. Meteoritics and Planetary Sciences, 37, 1729–1755.

Allen, J.M., Grossman, L., Lee, T., and Wasserburg, G.J. (1980) Mineralogy and petrography of HAL, an isotopically-unusual Allende inclusion. Geochimica et Cosmochimica Acta, 44, 685–699.

Armstrong, J.T. (1995) CITZAF—a package of correction programs for the quantitative electron microbeam X-ray-analysis of thick polished materials, thin-films, and particles. Microbeam Analysis, 4, 177–200.

Aroyo, M.I., Perez-Mato, J.M., Capillas, C., Kroumova, E., Ivantchev, S., Madariaga, G., Kirov, A., and Wondratschek, H. (2006) Bilbao Crystallographic Server: I. Databases and crystallographic computing programs. Zeitschrift für Kristallographie, 221, 15–27.

Ballirano, P. and Caminiti, R. (2001) Rietveld refinements on laboratory energy dispersive X-ray diffraction (EDXD) data. Journal of Applied Crystallography, 34, 757–762.

Bartos, A., Lieb, K.P., Uhrmacher, M., and Wiarda, D. (1993) Refinement of atomic positions in bixbyite oxides using perturbed angular correlation spectroscopy. Acta Crystallographica, B49, 165–169.

Barzilai, S., Halevy, I., and Yeheskel, O. (2011) Bulk modulus of Sc_2O_3: *Ab initio* calculations and experimental results. Journal of Applied Physics, 110, 043532.

Born, M. and Huang, K. (1954) Dynamical Theory of Crystal Lattices (1998 printing, p. 111). Oxford University Press, U.K.

Clarke, R.S., Jarosewich, E., Mason, B., Nelen, J., Gómez, M., and Hyde, J.R. (1971) The Allende, Mexico, meteorite shower. Smithsonian Contributions to Earth Science, 5, 1–53.

Dowty, E. (1987) Fully automated microcomputer calculation of vibrational spectra. Physics and Chemistry of Minerals, 14, 67–79.

El Goresy, A., Zinner, E., Matsunami, S., Palme, H., Spettel, B., Lin, Y., and Nazarov, M. (2002) Efremovka 101.1: A CAI with ultrarefractory REE patterns and enormous enrichments of Sc, Zr, and Y in fassaite and perovskite. Geochimica et Cosmochimica Acta, 66, 1459–1491.

Geller, S. (1971) Structures of α-Mn_2O_3, $(Mn_{0.983}Fe_{0.017})_2O_3$ and $(Mn_{0.37}Fe_{0.63})_2O_3$ and relation to magnetic ordering. Acta Crystallographica, B27, 821–828.

Hinton, R.W., Davis, A.M., Scatena-Wachel, D.E., Grossman, L., and Draus, R.J. (1988) A chemical and isotopic study of hibonite-rich refractory inclusions in primitive meteorites. Geochimica et Cosmochimica Acta, 52, 2573–2598.

Hiyagon, H. and Hashimoto, A. (1999) ^{16}O excesses in olivine inclusions in Yamato-86009 and Murchison chondrites and their relation to CAIs. Science, 283, 828–831.

Holland, T.J.B. and Redfern, S.A.T. (1997) Unit cell refinement from powder diffraction data: the use of regression diagnostics. Mineralogical Magazine, 61, 65–77.

Howard, C.J., Sabine, T.M., and Dickson, F. (1991) Structural and thermal parameters for rutile and anatase. Acta Crystallographica, B47, 462–468.

Kolitsch, U. and Tillmanns, E. (2003) Sc_2TiO_5, an entropy-stabilized pseudobrookite-type compound. Acta Crystallographica, E59, i36–i39.

Kraus, W. and Nolze, G. (1996) POWDER CELL – a program for the representation and manipulation of crystal structures and calculation of the resulting X-ray powder patterns. Journal of Applied Crystallography, 29, 301–303.

Krot, A.N., Petaev, M.I., Russell, S.S., Itoh, S., Fagan, T.J., Yurimoto, H., Chizmadia, L., Weisberg, M.K., Komatsu, M., Ulyanov, A.A., and Keil, K. (2004) Amoeboid olivine aggregates and related objects in carbonaceous chondrites: records of nebular and asteroid processes. Chemie der Erde, 64, 185–239.

Liu, W., Ice, G.E., Larson, B.C., Yang, W., Tischler, J.Z., and Budai, J.D. (2004) The three-dimensional X-ray crystal microscope: a new tool for materials characterization. Metallurgical and Materials Transactions A, 35A, 1963–1967.

Liu, W., Zschack, P., Tischler, J., Ice, G., and Larson, B. (2011) X-ray Laue diffraction microscopy in 3D at the Advanced Photon Source. 10th International Conference on X-ray Microscopy, 1365, AIP, p. 108–111. DOI: 10.1063/1.3625316.

Liu, X. and Liebermann, R.C. (1993) X-ray powder diffraction study of $CaTiO_3$ perovskite at high temperatures. Physics and Chemistry of Minerals, 20, 171–175.

Lodders, K. (2003) Solar system abundances and condensation temperatures of the elements. Astrophysical Journal, 591, 1220–1247.

Ma, C. (2011) Discovery of meteoritic lakargiite ($CaZrO_3$), a new ultra-refractory mineral from the Acfer 094 carbonaceous chondrite. Meteoritics & Planetary Science, 46, Supplement, A144.

Ma, C. and Rossman, G.R. (2008a) Barioperovskite, $BaTiO_3$, a new mineral from the Benitoite Mine, California. American Mineralogist, 93, 154–157.

——— (2008b) Discovery of tazheranite (cubic zirconia) in the Allende meteorite. Geochimica et Cosmochimica Acta, 72, 12S, A577.

——— (2009a) Tistarite, Ti_2O_3, a new refractory mineral from the Allende meteorite. American Mineralogist, 94, 841–844.

——— (2009b) Davisite, $CaScAlSiO_6$, a new pyroxene from the Allende meteorite. American Mineralogist, 94, 845–848.

Ma, C., Beckett, J.R., and Rossman, G.R. (2009) Allendeite and hexamolybdenum: Two new ultra-refractory minerals in Allende and two missing links. 40th Lunar and Planetary Science Conference, Abstract 1402.

Ma, C., Tschauner, O., Beckett, J.R., Kiefer, B., Rossman, G.R., and Liu, W. (2011a) Discovery of panguite, a new ultra-refractory titania mineral in Allende. 42nd Lunar and Planetary Science Conference, Abstract 1276.

Ma, C., Beckett, J.R., Tschauner, O., and Rossman, G.R. (2011b) Thortveitite ($Sc_2Si_2O_7$), the first solar silicate? Meteoritics & Planetary Science, 46, Supplement, A144.

Meagher, E.P. and Lager, G.A. (1979) Polyhedral thermal expansion in the TiO_2 polymorphs: Refinement of the crystal structures of rutile and brookite at high temperature. Canadian Mineralogist, 17, 77–85.

Nicolussi, G.K., Davis, A.M., Pellin, M.J., Lewis, R.S., Clayton, R.N., and Amari, S. (1997) s-process zirconium in presolar silicon carbide grains. Science, 277, 1281–1283.

Onoda, M. (1998) Phase transitions of Ti_3O_5. Journal of Solid State Chemistry, 136, 67–73.

Orobengoa, D., Capillas, C., Aroyo, M.I., and Perez-Mato, J.M. (2009) AMPLIMODES: symmetry-mode analysis on the Bilbao Crystallographic Server. Journal of Applied Crystallography, 42, 820–833.

Palko, J.W., Kriven, W.M., Sinogeikin, S.V., Bass, J.D., and Sayir, A. (2001) Elastic constants of yttria (Y_2O_3) monocrystals to high temperatures. Journal of Applied Physics, 89, 7791–7796.

Paque, J.M., Sutton, S.R., Simon, S.B., Beckett, J.R., Burnett, D.S., and Grossman, L. (2010) Valence of titanium in Ca-Al-rich inclusions: experimental samples and relevance to natural CAIs. Meteoritics & Planetary Science, 45, A161.

Perez-Mato, J.M., Orobengoa, D., and Aroyo, M.I. (2010) Mode crystallography of distorted structures. Acta Crystallographica, A66, 558–590.

Putz, H., Schön, J.C., and Jansen, M. (1999) Combined method for *ab initio* structure solution from powder diffraction data. Journal of Applied Crystallography, 32, 864–870.

Rastsvetaeva, R.K., Pushcharovskii, D.Yu., Spiridonov, E.M., and Gekimyants, V.M. (1998) Tazheranite and calzirtite: structural-mineralogical similarities and distinctions. Doklady Akademii Nauk SSSR, 359, 529–531.

Schleid, T. and Meyer, G. (1989) Single crystals of rare earth oxides from reducing halide melts. Journal of the Less-Common Metals, 149, 73–80.

Sheldrick, G.M. (2008) A short history of SHELX. Acta Crystallographica, A64, 112–122.

Tamura, N., Celestre, R.S., MacDowell, A.A., Padmore, H.A., Spolenak, R., Valek, B.C., Meier Chang, N., Manceau, A., and Patel, J.R. (2002) Submicron x-ray diffraction and its applications to problems in materials and environmental science. Review of Scientific Instruments, 73, 1369–1372.

Tamura, N., Padmore, H.A., and Patel, J.R. (2005) High spatial resolution stress measurements using synchrotron based scanning X-ray microdiffraction with white or monochromatic beam. Materials Science and Engineering, A, 399, 92–98.

Ubaldini, A. and Carnasciali, M.M. (2008) Raman characterisation of powder of cubic RE_2O_3 (RE = Nd, Gd, Dy, Tm, and Lu), Sc_2O_3 and Y_2O_3. Journal of Alloys and Compounds, 454, 374–378.

Vincent, M.G., Yvon, K., Grüttner, A., and Ashkenazi, J. (1980) Electron-density studies of metal-metal bonds. I. The deformation density of Ti_2O_3 at 295 K. Acta Crystallographica, A36, 803–808.

Wechsler, B.A. (1977) Cation distribution and high-temperature crystal chemistry of armalcolite. American Mineralogist, 62, 913–920.

Yang, H. and Hazen, R.M. (1999) Comparative high-pressure crystal chemistry of karrooite, $MgTi_2O_5$, with different ordering states. American Mineralogist, 84, 130–137.

Zhang, A. and Hsu, W. (2009) Refractory inclusions and aluminum-rich chondrules in Sayh al Uhaymir 290 CH chondrite: Petrography and mineralogy. Meteoritics and Planetary Science, 44, 787–804.

MANUSCRIPT RECEIVED OCTOBER 10, 2011
MANUSCRIPT ACCEPTED FEBRUARY 22, 2012
MANUSCRIPT HANDLED BY FERNANDO COLOMBO